# 3D motions in the Sculptor dwarf galaxy as a glimpse of a new era

D. Massari[1,2,*], M. A. Breddels[1], A. Helmi[1], L. Posti[1], A. G. A. Brown[2], E. Tolstoy[1]

[1] *Kapteyn Astronomical Institute, University of Groningen, PO Box 800, 9700 AV Groningen, The Netherlands*

[2] *Leiden Observatory, Leiden University, P.O. Box 9513, 2300 RA Leiden, The Netherlands*

**The 3D motions of stars in small galaxies beyond our own are minute yet they are crucial for understanding the nature of gravity and dark matter.[1,2] Even for the dwarf galaxy Sculptor –one of the best studied systems and inferred to be strongly dark matter dominated,[3,4] there are conflicting reports[5,6,7] on its mean motion around the Milky Way and the 3D internal motions of its stars have never been measured. Here we present precise proper motions of Sculptor's stars based on data from the Gaia mission[8] and the *Hubble Space Telescope*. Our measurements show that Sculptor moves around the Milky Way on a high-inclination elongated orbit that takes it much farther out than previously thought. For Sculptors internal velocity dispersions, we find $\sigma_R = 11.5 \pm 4.3$ km s$^{-1}$ and $\sigma_T = 8.5 \pm 3.2$ km s$^{-1}$ along the projected radial and tangential directions. Thus the stars in our sample move preferentially on radial orbits as quantified by the anisotropy parameter, which we find to be $\beta \sim 0.86^{+0.12}_{-0.83}$ at a location beyond the core radius. Taken at face value this high radial anisotropy requires abandoning conventional models[9] for Sculptors mass distribution. Our sample is dominated by metal-rich stars and for these we find $\beta^{MR} \sim 0.95^{+0.04}_{-0.27}$, a value consistent with multi-component spherical models where Sculptor is embedded in a cuspy dark halo[10] as might be expected for cold dark matter.**

To measure the proper motions (PMs) of individual stars in Sculptor we used data taken 12.27 years apart. The first epoch was acquired with the Advanced Camera for Surveys on board HST. The data set consists of two overlapping pointings separated by about $2'$ ($\sim 50$ pc, see Fig. 1), each split in several 400 sec exposures in the F775W filter. The overlapping field-of-view has been observed 11 times. We obtained a catalog of positions, instrumental magnitudes and Point Spread Function (PSF) fitting-quality parameters by treating each chip of each exposure independently. Stellar positions were corrected for filter-dependent geometric distortions.[11] We then cross-matched the single catalogs to compute $3\sigma$-clipped average positions, magnitudes and corresponding uncertainties. We built the complete HST

[*] Corresponding author: massariATastro.rug.nl

catalog after excluding all the saturated sources and those that were measured less than 4 times. The second epoch is provided by the *Gaia* first data release.[12] We extracted from the *Gaia* archive all sources in the direction of Sculptor.

We transformed the HST positions to the equatorial reference frame defined by the *Gaia* data (right ascension, RA, and declination, DEC), using a six-parameter linear transformation.[13] We found 126 stars in common and their PMs were computed as the difference between the *Gaia* and HST positions, divided by the temporal baseline. The uncertainties on the PMs were computed as the sum in quadrature between the *Gaia* and HST positional errors, divided by the temporal baseline, also taking into account the non-negligible correlations between *Gaia*'s RA and DEC uncertainties. After this first iteration, we repeated the procedure several times to compute the frame transformations using only likely members of Sculptor. These were selected using their location in the (G, G-$m_{F775W}$) color-magnitude diagram (Fig. 2a) and their previous PM determination. After three iterations, the number of selected stars stabilized at 91.

Our final catalog is shown in Fig. 2. Very distant objects such as background galaxies and quasars do not move and thus if present will have an apparent non-zero proper motion as a result of our procedure that sets Sculptor at rest.[14,15] Although there are no known quasars in our field of view, we were able to identify two background galaxies using the *Gaia* astrometric excess noise parameter,[16] and confirmed by eye (see Figs. 1b and 1c). Even though these are extended sources, their cores are well fit by a point source-like PSF, making them reliable for defining the absolute reference frame. The relative PMs measured for these two galaxies are red crosses in Fig. 2b. The fact that they both lie in the same region of this PM diagram supports our analysis. We adopted their weighted mean relative proper motion (blue cross in Fig. 2b) as the zero-point, thus the absolute PM for Sculptor is $(\mu_\alpha^{abs}\cos\delta,\ \mu_\delta^{abs})=(-0.20\pm0.14, -0.33\pm0.11)\ \mathrm{mas\,yr^{-1}}$, which corresponds to $(-79.6\pm55.7, -131.4\pm43.8)\ \mathrm{km\,s^{-1}}$ assuming a distance of $84\pm2$ kpc to Sculptor.[17] Fig. 2c shows that the motions of the stars in the field are coherent. Finally, Fig. 3 compares our PM measurement to previous estimates. It is not very surprising that none of the PMs agree with each other as the two previous astrometric measurements are based either on photographic plates[5] (known to suffer from strong systematic effects), or a much shorter (by a factor 6) temporal baseline.[6] The third estimate[7] was derived assuming that the line-of-sight velocity gradient observed in Sculptor is due to perspective effects ("apparent rotation"), which is incorrect in the presence of intrinsic rotation. More details and a thorough description of the extensive tests we have performed are reported in the Methods section.

To compute the orbit of Sculptor around the Milky Way and also to quantify the effect of "apparent rotation",[7] we combine our absolute PM measurement with literature values of the line of sight velocity[4] $v_{\rm los}$, distance,[17] and sky position of Sculptor. We use these as initial conditions (and also consider PMs within $1\sigma$ of the measured values) for the integration of orbits in a multi-component Galactic potential.[18] These show that Sculptor moves on a relatively high inclination orbit and that it is currently close to its minimum distance to the Milky Way, as we find its peri- and apocenter radii are $r_{\rm peri} = 73^{+8}_{-4}$ kpc and $r_{\rm apo} = 222^{+170}_{-80}$ kpc. The values of these orbital parameters depend on the assumed mass for the Milky Way halo, but variations of 30% lead to estimates within the quoted uncertainties (see the Methods section for more details).

Finally, we deduce the maximum apparent rotation for this orbit to be 2.5 $\rm km\,s^{-1}\,deg^{-1}$ at a position angle $\sim 18$ deg. Therefore if we correct the velocity gradient along the major axis previously measured[4] in Sculptor for this apparent rotation, we find an intrinsic rotation signal along this axis of amplitude 5.2 $\rm km\,s^{-1}\,deg^{-1}$. This implies that at its half-light radius, $v_{\rm rot}/\sigma_{\rm los} \sim 0.15$, for a line-of-sight velocity dispersion[4] $\sigma_{\rm los} = 10$ $\rm km\,s^{-1}$. Given the large pericentric distance and the small amount of rotation we have inferred, this implies that Sculptor did not originate in a disky dwarf that was tidally perturbed by the Milky Way.[19]

We determined the internal transverse motions of the stars in Sculptor using a sub-sample selected such that: (*i*) $18.4 < G < 19.1$ mag, to avoid stars in the HST non-linear regime and those where the *Gaia* positional errors are more uncertain;[20] (*ii*) the errors on each of the PM components are smaller than 0.07 $\rm mas\,yr^{-1}$(corresponding to 27.9 $\rm km\,s^{-1}$ at the distance of Sculptor); (*iii*) the total PM vector is smaller than 0.23 $\rm mas\,yr^{-1}$(i.e. 91.6 $\rm km\,s^{-1}$, this limit is set by the apparent PM of the background galaxies). There are 15 stars that satisfy these criteria and hence have the best PM measurements.

We model the velocity dispersion of this sample using a multivariate Gaussian. The parameters of this distribution are the mean velocities in the radial and tangential directions on the plane of the sky ($v_{0,R}, v_{0,T}$), the dispersions ($\sigma_R, \sigma_T$) and their correlation coefficient $\rho_{R,T}$. We use Bayes theorem to derive the posterior distribution for these parameters (assuming a Gaussian-like prior on the dispersions) from a Markov Chain Monte Carlo (MCMC) algorithm.[21] We find $\sigma_R = 11.5 \pm 4.3$ $\rm km\,s^{-1}$ and $\sigma_T = 8.5 \pm 3.2$ $\rm km\,s^{-1}$, as shown in Fig. 4a.

If we assume spherical symmetry and neglect rotation (see the Methods section for details), we can use the Jeans equations to find a relation[22] between the velocity dispersions measured at $R_{HST}$ (the location of our fields) and the value of the anisotropy $\hat{\beta} = \beta(\hat{r})$ where $\hat{r} \geq R_{HST}$:

$$\hat{\beta} = 1 - \frac{\sigma_T^2}{\sigma_{\rm los}^2 + \sigma_R^2 - \sigma_T^2}. \tag{1}$$

We determine $\sigma_{\rm los} \sim 6.9$ $\rm km\,s^{-1}$for 10 stars in common with a spectroscopic catalog.[23] Using the MCMC chain samples, we obtain the probability distribution for $\hat{\beta}$ shown in Fig. 4b. The two other histograms in this panel depict the results obtained assuming a flat-prior (dashed) or the more often quoted value $\sigma_{\rm los} \sim 10$ km s$^{-1}$(dotted). In all cases, radial anisotropy is clearly favored, with a median value $\hat{\beta} \sim 0.46$ and the maximum a posteriori $\hat{\beta}_{\rm MAP} \sim 0.86$.

This is the first ever determination of the value of the anisotropy $\beta$ in an external galaxy. The anisotropy is the key missing ingredient to robustly establish the distribution of matter in Sculptor, reflected in a longstanding unresolved debate,[24,25,26,10] as to whether or not this galaxy has the cuspy profile[27] predicted by the concordance cosmological model in which dark matter is cold, constituted by weakly interacting particles.[2]

The value of $\beta$ we have measured is surprising. A review[9] of the literature indicates that most previous works have assumed spherical symmetry and derived, for a variety of mass models of Sculptor, $\beta \leq 0$ for $\beta$ constant with radius. However, no physical system can have a constant anisotropy and $\beta \sim 0.8$ with a light density profile that has a central slope $\gamma(0) \sim 0$, since $\gamma$ has to satisfy $\gamma \geq 2\beta$ in the spherically symmetric limit.[28] Therefore, in this context, our result shows that the anisotropy in Sculptor cannot be constant with radius. Our measurement also rules out the simplest predictions for Sculptor's anisotropy based on the alternative gravity model known as MOND.[29]

Our results highlight the necessity to go beyond the standard assumptions. We may need to consider that Sculptor's dark halo may be axisymmetric or even triaxial. Alternatively and quite plausibly our measurement may be biased towards the colder, more centrally concentrated, metal-rich(er) subcomponent of Sculptor.[4] Of the 15 stars in our best PM sample, 9 have a metallicity measurement[23] (see Methods section for details) and 6 of these have [Fe/H]$> -1.4$ dex, indicating that about half could belong to this subcomponent of Sculptor. From the 11 stars in our sample with [Fe/H]$> -1.4$ dex, $18.4 \leq G \leq 21$, and that satisfy also the quality criteria, we determine the anisotropy to be clearly radial with $\hat{\beta}^{MR}_{\rm MAP} = 0.95^{+0.04}_{-0.27}$ and a median $\hat{\beta}^{MR} = 0.82$ at a distance $\hat{r} \geq R_{HST}$, as shown in Fig. 4c. This value is in excellent agreement[10] with predictions if Sculptor's metal-rich component is embedded in a spherical cuspy dark halo profile. It remains to be seen if such a high value can also be consistent with cored models, since those published[4,25] typically predict lower, though still radial, anisotropy, or with non-spherical models, which have thus far remained largely unexplored. Another intriguing question is what formation mechanism produces a population of stars moving on such very elongated orbits.

## REFERENCES

[1] Lin, D. N. C., & Faber, S. M. Some implications of nonluminous matter in dwarf spheroidal galaxies, *Astrophys. J. Lett.* **266**, 21-25 (1983).

[2] Strigari, L. E. Galactic searches for dark matter, *Phys. Rep.* **531**, 1-88 (2013).

[3] Walker, M. G., Mateo, M., Olszewski, E. W., et al. Velocity Dispersion Profiles of Seven Dwarf Spheroidal Galaxies, *Astrophys. J. Lett.* **667**, 53-56 (2007).

[4] Battaglia, G., Helmi, A., Tolstoy, E., et al. The Kinematic Status and Mass Content of the Sculptor Dwarf Spheroidal Galaxy, *Astrophys. J. Lett.* **681**, (2008).

[5] Schweitzer, A. E., Cudworth, K. M., Majewski, S. R., & Suntzeff, N. B. The Absolute Proper Motion and a Membership Survey of the Sculptor Dwarf Spheroidal Galaxy, *Astron. J.* **110**, 2747-2757 (1995).

[6] Piatek, S., Pryor, C., Bristow, P., et al. Proper Motions of Dwarf Spheroidal Galaxies from Hubble Space Telescope Imaging. IV. Measurement for Sculptor, *Astron. J.* **131**, 1445-1460 (2006).

[7] Walker, M. G., Mateo, M., & Olszewski, E. W. Systemic Proper Motions of Milky Way Satellites from Stellar Redshifts: The Carina, Fornax, Sculptor, and Sextans Dwarf Spheroidals, *Astrophys. J. Lett.* **688**, (2008).

[8] Gaia Collaboration, Prusti, T., de Bruijne, J. H. J., et al. The Gaia mission, *Astron. Astrophys.* **595**, (2016).

[9] as reviewed in Battaglia, G., Helmi, A., & Breddels, M. Internal kinematics and dynamical models of dwarf spheroidal galaxies around the Milky Way, *New Astron. Rev.* **57**, 52-79 (2013).

[10] Strigari, L. E., Frenk, C. S., & White, S. D. M. Dynamical Models for the Sculptor Dwarf Spheroidal in a CDM Universe, *Astrophys. J.* **838**, 123-132 (2017).

[11] Anderson, J. Variation of the Distortion Solution, *Inst. Sci. Rep. ACS 2007-08* **8**, (2007).

[12] Gaia Collaboration, Brown, A. G. A., Vallenari, A., et al. Gaia Data Release 1. Summary of the astrometric, photometric, and survey properties, *Astron. Astrophys.* **595**, (2016).

[13] Massari, D., Posti, L., Helmi, A., Fiorentino, G., & Tolstoy, E. The power of teaming up HST and Gaia: the first proper motion measurement of the distant cluster NGC 2419, *Astron. Astrophys.* **598**, (2017).

[14] Dinescu, D. I., Girard, T. M., & van Altena, W. F. Space Velocities of Globular Clusters. III. Cluster Orbits and Halo Substructure, *Astron. J.* **117**, 1792-1815 (1999).

[15] Sohn, S. T., Anderson, J., & van der Marel, R. P. The M31 Velocity Vector. I. Hubble Space Telescope Proper-motion Measurements, *Astrophys. J.* **753**, (2012).

[16] Lindegren, L., Lammers, U., Bastian, U., et al. Gaia Data Release 1. Astrometry: one billion positions, two million proper motions and parallaxes, *Astron. Astrophys.* **595**, (2016).

[17] Martínez-Vázquez, C. E., Monelli, M., Bono, G., et al. Variable stars in Local Group Galaxies - I. Tracing the early chemical enrichment and radial gradients in the Sculptor dSph with RR Lyrae stars, *Mon. Not. R. Astron. Soc.* **454**, 1509-1516 (2015).

[18] Piffl, T., Binney, J., McMillan, P. J., et al. Constraining the Galaxy's dark halo with RAVE stars, *Mon. Not. R. Astron. Soc.* **445**, 3133-3151 (2014).

[19] Mayer, L., Governato, F., Colpi, M., et al. The Metamorphosis of Tidally Stirred Dwarf Galaxies, *Astrophys. J.* **559**, 754-784 (2001).

[20] Michalik, D., Lindegren, L., Hobbs, D., & Butkevich, A. G. Gaia astrometry for stars with too few observations. A Bayesian approach, *Astron. Astrophys.* **583**, (2015).

[21] Foreman-Mackey, D., Hogg, D. W., Lang, D., & Goodman, J. emcee: The MCMC Hammer, *Public. Astron. Soc. Pac.* **125**, 306-312 (2013).

[22] Strigari, L. E., Bullock, J. S., & Kaplinghat, M. Determining the Nature of Dark Matter with Astrometry, *Astrophys. J. Lett.* **657**, 1-4 (2007).

[23] Walker, M. G., Mateo, M., & Olszewski, E. W. Stellar Velocities in the Carina, Fornax, Sculptor, and Sextans dSph Galaxies: Data From the Magellan/MMFS Survey, *Astron. J.* **137**, 3100-3108 (2009).

[24] Walker, M. G., & Peñarrubia, J. A Method for Measuring (Slopes of) the Mass Profiles of Dwarf Spheroidal Galaxies, *Astrophys. J.* **742**, (2011).

[25] Amorisco, N. C., & Evans, N. W. Dark matter cores and cusps: the case of multiple stellar populations in dwarf spheroidals, *Mon. Not. R. Astron. Soc.* **419**, 184-196 (2012).

[26] Breddels, M. A., & Helmi, A. Model comparison of the dark matter profiles of Fornax, Sculptor, Carina and Sextans, *Astron. Astrophys.* **558**, (2013).

[27] Navarro, J. F., Frenk, C. S., & White, S. D. M. The Structure of Cold Dark Matter Halos, *Astrophys. J.* **462**, 563-575 (1996).

[28] An, J. H., & Evans, N. W. A Cusp Slope-Central Anisotropy Theorem, *Astrophys. J.* **642**, 752-758 (2006).

[29] Angus, G. W. Dwarf spheroidals in MOND, *Mon. Not. R. Astron. Soc.* **387**, 1481-1488 (2008).

[30] Irwin, M., & Hatzidimitriou, D. Structural parameters for the Galactic dwarf spheroidals, *Mon. Not. R. Astron. Soc.* **277**, 1354-1378 (1995).

**Supplementary Information** is linked to the online version of the paper at www.nature.com/nature.

**Acknowledgements:** We thank the anonymous referees for their comments and suggestions which improved the presentation and interpretation of our results. We have made use of data from the European Space Agency mission *Gaia* (`http://www.cosmos.esa.int/gaia`), processed by the *Gaia* Data Processing and Analysis Consortium (DPAC, `http://www.cosmos.esa.int` Funding for DPAC has been provided by national institutions, in particular the institutions participating in the *Gaia* Multilateral Agreement. This work is also based on observations made with the NASA/ESA Hubble Space Telescope, obtained from the Data Archive at the Space Telescope Science Institute, which is operated by the Association of Universities for Research in Astronomy, Inc., under NASA contract NAS 5-26555. A.H. and L.P. acknowledge financial support from a Vici grant from the Netherlands Organisation for Scientific Research. M.B. and A.H. are grateful to NOVA for financial support.

**Authors' contributions:** D.M. performed the data analysis and the proper motion measurements, M.B. developed the statistical tools, A.H. derived the relations between observables and orbital anisotropy, coordinated the work and led the scientific interpretation, L.P. performed the orbit computation, A.B. and E.T. contributed to the presentation of the paper. All the authors critically contributed to the work presented here.

**Authors' information** Reprints and permissions information is available at `www.nature.com/reprints`. The authors declare no competing financial interests. Readers are welcome to comment on the online version of the paper. Publishers note: Springer Nature remains neutral with regard to jurisdictional claims in published maps and institutional affiliations. Correspondence and requests for materials should be addressed to D.M. (massari@astro.rug.nl) or A.H. (helmi@astro.rug.nl)

This preprint was prepared with the AAS LaTeX macros v5.2.

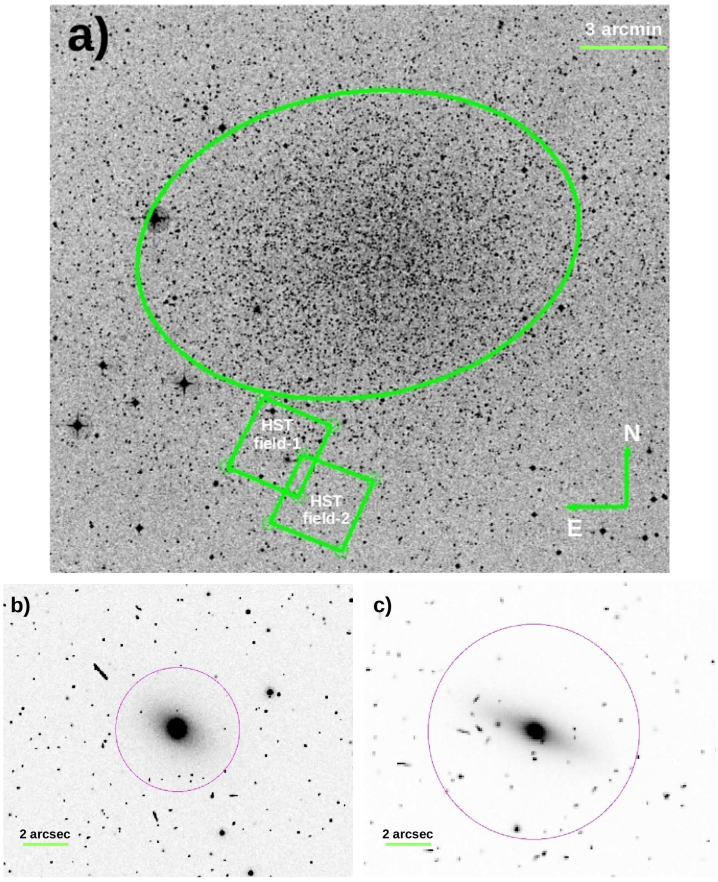


Fig. 1.— **Field of view towards the Sculptor dwarf spheroidal galaxy.** a) is a Digital Sky Survey image of the center of Sculptor. The ellipse indicates the core radius[30] ($r_c \sim 5.9' \sim 144$ pc). The two HST pointings marked with boxes are located at an average distance $R_{HST} \sim 7.6' \sim 185$ pc, well inside the half-light radius ($\mathrm{r}_{hl} \sim 16' \sim 390$ pc) of the system. b) and c) show the HST images of the two background galaxies (enclosed within purple circles) used to determine the absolute zero point of the PM.

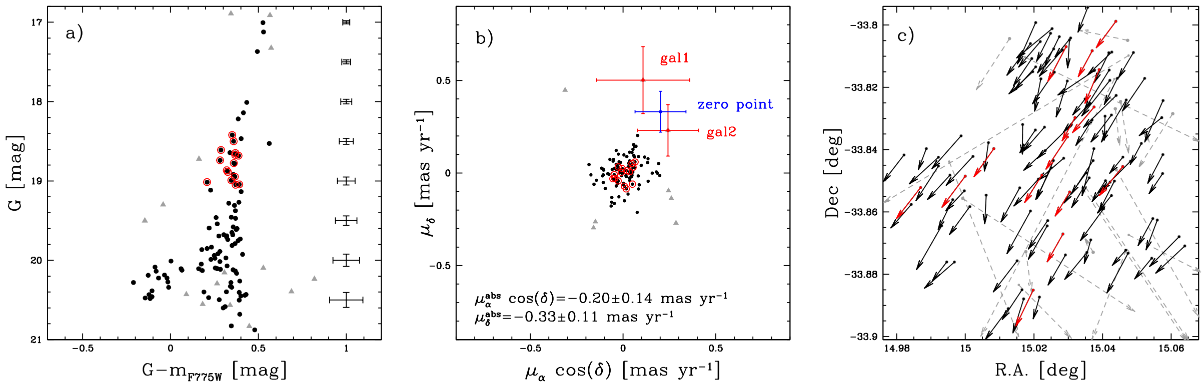


Fig. 2.— **Properties of our sample.** a) is the color-magnitude diagram for the stars in our PM catalog. G magnitudes are in the Gaia photometric system, $m_{F775W}$ magnitudes in the VEGAmag system ($1\sigma$ errorbars are shown on the right). Black dots are likely members (with PM amplitude smaller than 0.23 mas yr$^{-1}$), red circles are the 15 member stars with the best measured PMs (used to compute the internal velocity dispersion of Sculptor, see the text for the details of the selection), and gray triangles are likely non-members. The same color coding is used in the next panels. b) shows the sources with a measured PM. The two background galaxies are marked in red, and their weighted mean in blue, together with the associated $1\sigma$ uncertainty. c) shows the observed projected motions of stars in the field.

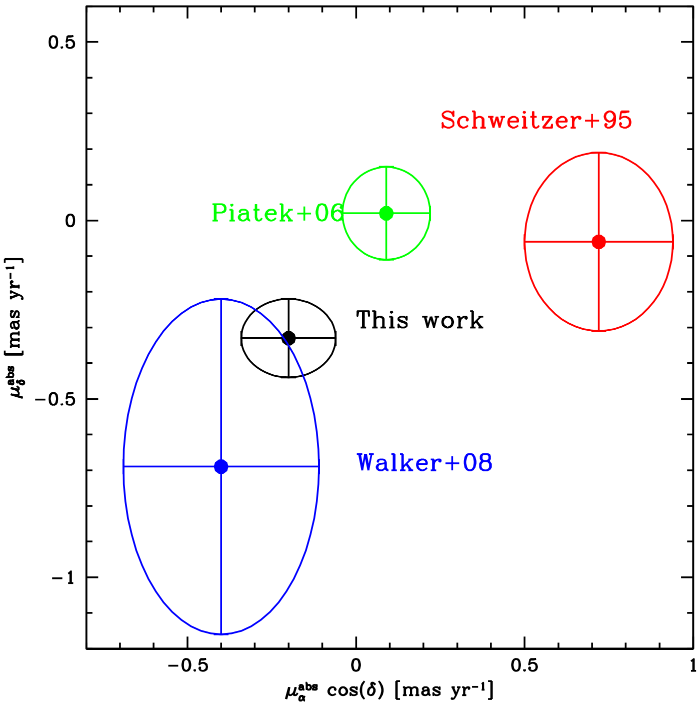


Fig. 3.— **Comparison to previously published PM estimates for Sculptor**. Each ellipse denotes the 68% confidence level. The first estimate is based either on photographic plates[5] (red ellipse), the second used a $\sim 2$ years temporal baseline[6] (green ellipse), while the third estimate[7] (blue ellipse) assumed that the line-of-sight velocity gradient observed in Sculptor is due to perspective effects.

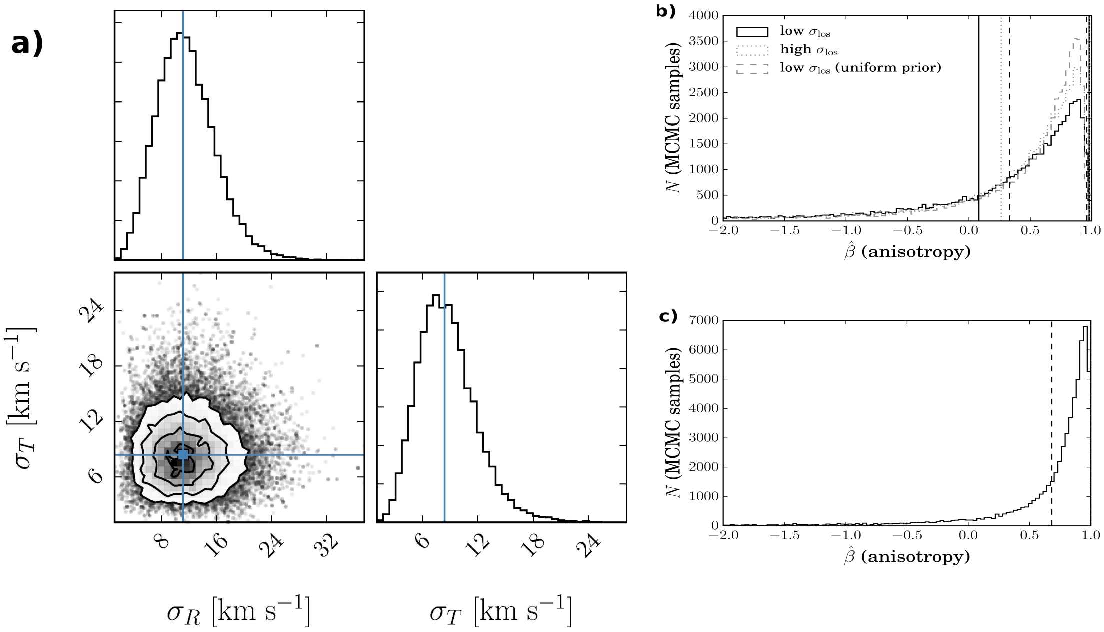


Fig. 4.— **2D velocity dispersion and orbital anisotropy of Sculptor.** a) shows the posterior probability distribution for the projected velocity dispersions $\sigma_R$ and $\sigma_T$ for the sample of 15 stars with the best PM measurements. Their maximum a posteriori (MAP) values are indicated with the solid (blue) lines. The y-axis of the histograms indicate the number of MCMC samples. b) shows the resulting distribution of the anisotropy parameter $\hat{\beta}$ at a radius $\hat{r} \geq R_{HST}$, where $R_{HST} \sim 7.6'$ is the average projected distance of stars from the center of Sculptor. The solid and dashed histograms are computed using $\sigma_{\rm los}$ for these stars (assuming a Gaussian and flat priors respectively), and the dotted histogram is for a more commonly used value of $\sigma_{\rm los} = 10$ km s$^{-1}$. The MAP values for the anisotropy are, for the low $\sigma_{\rm los}$, $\hat{\beta}_{\rm MAP} = 0.86^{+0.12}_{-0.83}$ (Gaussian prior), $\hat{\beta}_{\rm MAP} = 0.83^{+0.14}_{-0.55}$ (flat prior), and $\hat{\beta}_{\rm MAP} = 0.86^{+0.09}_{-0.64}$ for the high $\sigma_{\rm los}$. c) shows the posterior probability distribution for $\hat{\beta}$ for the metal-rich subsample, using their $\sigma_{\rm los}$. The vertical lines in panels b) and c) mark the 68% highest posterior density intervals around the MAP values.

**Methods Section**

## 1. Description of the HST data and procedures

To measure the proper motions (PMs) of stars in the Sculptor dwarf spheroidal galaxy we used two epochs of data obtained with the two best astrometric space facilities available at the moment: the HST and the *Gaia* mission. The first epoch of observations was acquired with the Wide Field Channel (WFC) of the Advanced Camera for Survey (ACS) on board the HST. This camera is made up of two $2048 \times 4096$ pixel detectors separated by a gap of about 50 pixels. Its pixel scale is $\sim 0.05''$ pixel$^{-1}$, for a total field of view (FoV) $\sim 200'' \times 200''$. The data set (GO-9480, PI: Rhodes), consists of two overlapping pointings separated by about $2'$. In turn, the first pointing is split in five 400 sec long exposure images in the F775W filter. The second pointing is made up of six exposures with the same characteristics. The overlapping FoV has thus been observed 11 times. This data set has been acquired on the 26th of September, 2002.

We retrieved from the archive only _FLC images, which are corrected for charge transfer efficiency (CTE) losses by the pre-reduction pipeline adopting a pixel-based correction.[31,32] The data-reduction was performed with the `img2xym_WFC.09×10` program.[33] We treated each chip of each exposure independently, and we obtained a catalog with positions, instrumental magnitudes and Point Spread Function (PSF) fitting-quality parameter for each of them. Stellar positions were corrected for filter-dependent geometric distortions[11]. We then cross-matched the single catalogs to compute $3\sigma$-clipped average positions, magnitudes and corresponding uncertainties (defined as the rms of the residuals around the mean value). We finally built the total HST catalog after excluding all the saturated sources and those that were measured less than 4 times.

## 2. Error analysis

Since for this study a good control of all the uncertainties is fundamental, in the following we summarize every source of measurement error in an attempt to find and correct possible unaccounted for terms.

## 2.1. Intrinsic errors

### *2.1.1. HST*

From the analysis of many HST dithered images, a general trend for the behavior of ACS/WFC single exposures positional errors as a function of instrumental magnitude and adopted filter has been derived.[34] This trend has been modeled for three filters (F435W, F606W and F814W), but very similar results were found for all of them, and especially for the two redder ones. Our exposures have been observed in the filter F775W (instrumental magnitudes were calibrated onto the VEGAmag system using publicly available aperture corrections and zeropoints, at `http://www.stsci.edu/hst/acs/analysis/zeropoints.`), so that it is reasonable to compare the positional errors we obtained with the model describing F606W and F814W. Such a comparison is shown in Supplementary Fig. 1. To compute our single-exposure positional errors, we multiplied the rms values in the HST global catalog obtained as described above, by sqrt($N$), where $N$ is the number of times each star has been measured.

Single-exposure errors computed in this way still contain another source of uncertainty given by possible residuals in the geometric distortion solution. It has been reported[35] that the distortion solution for the F775W filter is slightly worse than e.g. that for the F606W filter because of the lower number of images available used for modeling. The expected residuals should be of the order of 0.01 pixels.[35] Indeed, this explains very well why our errors are located systematically above the expectation given by the red solid line in Supplementary Fig. 1. By adding in quadrature an additional term of $\sim$ 0.01 pixels, which mimics the effect of distortion residuals, the expected trend (dashed red line) matches well the median behavior obtained from our data. Therefore, we conclude that the estimated errors for the HST first-epoch position are reasonable and robust.

### *2.1.2. Gaia*

The *Gaia* positional uncertainties and correlations have been extensively analyzed and discussed in the recent literature[17,36]. Their determination will certainly improve in the next data releases, but they are currently in the best shape allowed by the amount of data collected so far. We therefore take the errors at their face value.

## 2.2. Systematic uncertainties

PM measurements can be affected by several systematic uncertainties. In the following we test our measurements against a comprehensive list of systematic effects, based on the prescriptions described in previous work.[34]

*Chromatic effects.* Differential chromatic refraction[37] (DCR) is one of the most common sources of systematic uncertainties on astrometric measurements. This is due to the fact that DCR shifts the position of photons on the detector proportionally to their wavelength and to the zenithal angle of the observations. Since this effect is induced by the atmosphere, our data taken from space facilities should be unaffected, but possible chromatic effects could still play a role. We checked for this by looking for trends of our PMs as a function of color (G-$m_{F775W}$). As evident in the top panel of Supplementary Fig. 2 (where the two PM components $\mu_\alpha \cos(\delta)$ and $\mu_\delta$ are shown with black and red symbols, respectively) no such trends are apparent. In fact the best least squares linear fit, $\mu = a_\mu + b_\mu(G - m_{F775W})$, has coefficients that are consistent with zero within $1\sigma$ (e.g $b_{\mu\alpha_*} = 0.01 \pm 0.09$ mas yr$^{-1}$ mag$^{-1}$and $b_{\mu\delta} = -0.03 \pm 0.09$ mas yr$^{-1}$ mag$^{-1}$). We can therefore rule out the presence of systematic chromatic effects affecting our PMs.

*CTE losses.* Defects in the silicon lattice of the ACS detector can lead to an inefficient read-out of the charge that causes deferred-charge trails developing from each source along the vertical direction.[32] This effects tends to systematically move the centroid of sources in the same (vertical) direction, and more significantly affects faint objects.[38] The images we used in this study have already been corrected for CTE losses, but we further checked for the existence of possible residuals by looking for trends among our measured PMs and magnitude (faint stars should be more affected) and positions (trends along the ACS Y-direction should be observed). The first of these tests is shown in the bottom panel of Supplementary Fig. 2, where the two PM components are plotted against *Gaia* G-band magnitudes. As in the previous case, no trend is found (the slopes being $b_{\mu\alpha*} = -0.02 \pm 0.08$ mas yr$^{-1}$ mag$^{-1}$and $b_{\mu\delta} = -0.01 \pm 0.09$ mas yr$^{-1}$ mag$^{-1}$). The second test is shown in Supplementary Fig. 3. We rotated the PMs by 24.75 degrees, such that their X- and Y- components correspond to the horizontal and vertical direction of the ACS detector. Again, in all cases the slopes of the best linear fit are fully consistent with zero, i.e. no trends are apparent. We can then conclude that residuals CTE effects are not affecting our measurements.

*Other systematic effects.* In general, other not well identified systematic effects could affect our PM measurements or their estimated uncertainties. We checked for their presence by looking for trends between PMs and all the other measured quantities (photometric parameters, positions, quality of the PSF fitting, astrometric excess noise), finding none. Therefore, after this analysis we can conclude that our PM measurements do not suffer from (the better) known systematic effects.

Possible global systemic motions of the dSph like expansion/contraction or rotation on the plane of the sky could translate into systematic uncertainties on our absolute PM estimate. However, given the large distance of Sculptor (we adopt throughout the paper a distance of 84 kpc, obtained from the analysis of RR Lyrae variable stars[18]), they are negligible compared to the uncertainty on the absolute zero-point. For example, if we assume that the total rotational signal of 7.6 $\mathrm{km\,s^{-1}\,deg^{-1}}$ reported in the literature[4] corresponds to rotation on the plane of the sky, then the corresponding PM at the location of our HST FoV would be of only 0.003 $\mathrm{mas\,yr^{-1}}$.

## 3. The orbit of Sculptor around the Milky Way and its apparent rotation

We use the observed position on the sky, distance, heliocentric radial velocity and our newly obtained PM measurements of Sculptor to derive its orbit. In a right-handed Cartesian heliocentric reference frame, where $X$ points towards the Galactic center, $Y$ in the direction of rotation and $Z$ is positive towards the Galactic North pole, Sculptor lies at $(X, Y, Z) = (3, -9.5, -83.4)$ kpc and moves with velocity $(V_X, V_Y, V_Z) = (143.3, -76, -90.3)$ $\mathrm{km\,s^{-1}}$. We then correct for the Sun's position and velocity w.r.t. the Galactic center[40] assuming $(X_\odot, Y_\odot, Z_\odot) = (-8.3, 0, 0.014)$ kpc, and $(V_{X,\odot}, V_{Y,\odot}, V_{Z,\odot}) = (11.1, 240.24, 7.25)$ $\mathrm{km\,s^{-1}}$. We integrate these initial conditions, together with 100 random realizations assuming that the errors in the observables are Gaussian, in an axisymmetric Galactic potential for 4 Gyr forward and backward in time using an $8^{th}$ order Runge-Kutta method. The Galactic potential[19] has several components: a flattened bulge, a gaseous exponential disc, thin and thick stellar exponential discs and a flattened ($q = 0.8$) dark matter halo. The total baryonic (stars and cold gas) mass of the model is $M_{\rm bary} = 5.3 \times 10^{10}\,\mathrm{M_\odot}$, while the dark halo follows an NFW[28] profile whose virial mass is $M_{200} = 1.3 \times 10^{12}\,\mathrm{M_\odot}$ and its concentration $c_{200} = 20$. As reported in the main part of the paper, we find that Sculptor has recently (approximately 170 Myr ago) reached its minimum distance to the Milky Way, and is currently moving outwards. The peri- and apocenter radii are $r_{\rm peri} = 73^{+8}_{-4}$ kpc and $r_{\rm apo} = 222^{+170}_{-80}$ kpc, and the orbit has a relatively high inclination of 88 deg. These values are, of course dependent on the characteristic parameters of the Galactic potential. To give a flavor of how they change we vary the mass of the Milky Way halo by 30%. We find that for $M_{200} = 0.9 \times 10^{12}\,\mathrm{M_\odot}$, then $r_{\rm peri} = 83^{+2}_{-10}$ kpc and $r_{\rm apo} = 475^{+210}_{-175}$ kpc, while for $M_{200} = 1.7 \times 10^{12}\,\mathrm{M_\odot}$, $r_{\rm peri} = 73^{+3}_{-2}$ kpc and $r_{\rm apo} = 143^{+34}_{-21}$ kpc. As expected, only the apocentric distance varies strongly with $M_{200}$. In fact, if we assume $M_{200}$ to be half of our fiducial value (i.e. $0.65 \times 10^{12}\,\mathrm{M_\odot}$), then Sculptor would be unbound.

Now that we have determined the orbital motion of Sculptor, we may quantify the magnitude of the "apparent" rotation. The total apparent velocity field induced by the orbit is shown in Supplementary Fig. 4, where the black ellipse corresponds to the tidal radius of Sculptor[13] and the direction of its PM is indicated by the black arrow. The velocity field, color-coded in steps of 0.5 $\mathrm{km\,s^{-1}}$, has a maximum magnitude of 2.5 $\mathrm{km\,s^{-1}\,deg^{-1}}$at PA $\simeq 18\,\mathrm{deg}$, that is projected to an apparent velocity gradient of 2.4 $\mathrm{km\,s^{-1}\,deg^{-1}}$ along the major axis and 0.7 $\mathrm{km\,s^{-1}\,deg^{-1}}$ along the minor axis.

## 4. Velocity dispersion and anisotropy

In this section we describe the procedure for deriving the velocity dispersion on the plane of the sky as well as the velocity anisotropy of Sculptor.

We transform the PM components from the equatorial reference to radial and tangential components on the plane of the sky according to the equatorial-polar coordinates relation:[41]

$$\begin{bmatrix} \mu_R \\ \mu_T \end{bmatrix} = \begin{bmatrix} \cos(\phi) & \sin(\phi) \\ -\sin(\phi) & \cos(\phi) \end{bmatrix} \times \begin{bmatrix} \mu_\alpha \cos(\delta) \\ \mu_\delta \end{bmatrix},$$

where $\phi = \arctan(y/x)$, and $x$ and $y$ are the (local Cartesian) gnomonic projected coordinates. Uncertainties are fully propagated taking into account the correlation coefficient between *Gaia* 's RA and DEC estimates. The projected velocities in the radial and tangential direction therefore are $v_{R,T} = 4.74\mu_{R,T}d$, with $d$ the distance to Sculptor.

We model the velocity dispersion for the sample selected as described in the main body of the paper, by a multivariate Gaussian including a covariance term. This Gaussian is characterized by velocity dispersions in the (projected) radial and tangential directions $(\sigma_R, \sigma_T)$, their correlation coefficient $\rho_{R,T}$ and the mean velocities $(v_{0,R}, v_{0,T})$. The posterior for these parameters $\mathbf{p} = (\sigma_R, \sigma_T, v_{0,R}, v_{0,T}, \rho_{R,T})$, including the data $D$, is given by Bayes theorem:

$$p(\sigma_R, \sigma_T, v_{0,R}, v_{0,T}, \rho_{R,T}|D) = p(D|\sigma_R, \sigma_T, v_{0,R}, v_{0,T}, \rho_{R,T})p(\sigma_R, \sigma_T, v_{0,R}, v_{0,T}, \rho_{R,T})/p(D). \tag{2}$$

The likelihood here, $p(D|\mathbf{p})$, is a product of Gaussians, $\mathcal{N}$, and the covariance matrix is the sum of the covariance matrices associated to the intrinsic kinematics of the population and to the measurement uncertainties (which is equivalent to a convolution of the two Gaussians representing these contributions), i.e.

$$p(D|\sigma_R, \sigma_T, v_{0,R}, v_{0,T}, \rho_{R,T}) = \prod_i \mathcal{N}\left( \begin{bmatrix} v_{R,i} \\ v_{T,i} \end{bmatrix}, \begin{bmatrix} v_{0,R} \\ v_{0,T} \end{bmatrix}, \Sigma_i \right), \tag{3}$$

$$\Sigma_i = \begin{bmatrix} \sigma_R^2 & \rho_{R,T}\sigma_R\sigma_T \\ \rho_{R,T}\sigma_R\sigma_T & \sigma_T^2 \end{bmatrix} + \begin{bmatrix} \epsilon^2_{\sigma_R,i} & \rho_{R_i,T_i}\epsilon_{\sigma_R,i}\epsilon_{\sigma_T,i} \\ \rho_{R_i,T_i}\epsilon_{\sigma_R,i}\epsilon_{\sigma_T,i} & \epsilon^2_{\sigma_T,i}. \end{bmatrix} \tag{4}$$

Furthermore, for the prior $p(\mathbf{p})$ in Eq. (2), we assume it has a weak Gaussian-like form for the correlation coefficient of the intrinsic kinematics of the population (with mean 0, and dispersion 0.8) while a flat prior is assumed for the mean velocities. We explore two different priors for the velocity dispersion: a Gaussian-like for the (logarithm of the) velocity dispersions (with mean $\log_{10} 12[\mathrm{km\,s^{-1}}]$, and unity dispersion), and a uniform prior.

We have used a Markov Chain Monte Carlo (MCMC) algorithm[22] to estimate the posterior all the parameters, but, except for $\sigma_R$ and $\sigma_T$, we consider all as nuisance parameters. As reported in the main body of the paper, we find for our best PM sample $\sigma_R = 11.5 \pm 4.3\ \mathrm{km\,s^{-1}}$ and $\sigma_T = 8.5 \pm 3.2\ \mathrm{km\,s^{-1}}$ in the case of the Gaussian prior (similar values are obtained for the flat case).

In our analysis we have left the mean projected velocities $v_{0,R}$ and $v_{0,T}$ as free (nuisance) parameters, and find values entirely consistent with those determined in the main body of the paper. If Sculptor would rotate with an amplitude of 5.2 $\mathrm{km\,s^{-1}\,deg^{-1}}$, this would induce a gradient in the field where our stars are found of order 0.5 $\mathrm{km\,s^{-1}}$, that therefore would be negligible.

The anisotropy $\beta(r)$ provides a measure of the intrinsic orbital distribution of the system, and is defined as $\beta = 1 - \dfrac{\sigma_t^2}{2\sigma_r^2}$, where $\sigma_t$ and $\sigma_r$ are the intrinsic (3D) velocity dispersions in the tangential and radial directions, respectively. To obtain an estimate of the orbital anisotropy $\beta$ from the observables $\sigma_{\rm los}$, $\sigma_R$ and $\sigma_T$ we use the spherical Jeans equations. These link the measured dispersions with intrinsic properties of the system, namely $\sigma_r(r)$, $\beta(r)$, and the light density profile ($\nu_*(r)$ in 3D and projected $I_*(R)$) as follows[23]:

$$\sigma^2_{\rm los}(R) = \frac{2}{I_\star(R)} \int_R^\infty \left(1 - \beta\frac{R^2}{r^2}\right) \frac{\nu_\star \sigma_r^2 r dr}{\sqrt{r^2 - R^2}}, \tag{5}$$

$$\sigma^2_R(R) = \frac{2}{I_\star(R)} \int_R^\infty \left(1 - \beta + \beta\frac{R^2}{r^2}\right) \frac{\nu_\star \sigma_r^2 r dr}{\sqrt{r^2 - R^2}}, \tag{6}$$

$$\sigma^2_T(R) = \frac{2}{I_\star(R)} \int_R^\infty (1 - \beta) \frac{\nu_\star \sigma_r^2 r dr}{\sqrt{r^2 - R^2}}. \tag{7}$$

If we define $Q(r) = \nu_\star \sigma_r^2 r/\sqrt{r^2 - R^2}$, and

$$f_1(R) = \int_R^\infty Q(r)dr, \qquad f_2(R) = \int_R^\infty \beta(r)\frac{R^2}{r^2}Q(r)dr, \qquad f_3(R) = \int_R^\infty \beta(r)Q(r)dr,$$

then

$$\begin{aligned}
\sigma_{\rm los}^2(R) &= \frac{2}{I_\star(R)}(f_1(R) - f_2(R)), \\
\sigma_R^2(R) &= \frac{2}{I_\star(R)}(f_1(R) - f_3(R) + f_2(R)), \\
\sigma_T^2(R) &= \frac{2}{I_\star(R)}(f_1(R) - f_3(R)).
\end{aligned}$$

If we do not make any assumptions on $\beta(r)$, we may use the mean value theorem in the form

$$\int_a^b f(x)g(x)dx = f(c)\int_a^b g(x)dx, \qquad c \in [a, b],$$

which holds provided $g(x)$ does not change sign in $[a, b]$. In our case we could apply this theorem to say that $\exists\, \hat{r} \in [R_{HST}, \infty)$ such that $f_3(R_{HST}) = \hat{\beta} f_1(R_{HST})$, where $R_{HST}$ is the location where we have measured the velocity dispersions $\sigma_R$ and $\sigma_T$ with our dataset. This means that

$$\hat{\beta} = \beta(\hat{r}) = 1 - \frac{\sigma_T^2}{\sigma_{\rm los}^2 + \sigma_R^2 - \sigma_T^2}, \qquad \text{with } \hat{r} \in [R_{HST}, r_{\rm max}), \tag{8}$$

where we have used that in reality, Sculptor has a maximum (finite) radial extent which we denote by $r_{\rm max}$. Note that if $\beta$ is constant, then Eq. (8) holds at every radius.

As discussed in the main body of the paper, there are indications that our sample may be dominated by metal-rich stars, a component known to have its own characteristic spatial distribution and kinematics.[42] To derive the metallicity of our stars, we took the measured iron spectral index ΣFe reported in the spectroscopic sample observed with the MIKE spectrograph at the Magellan 6.5m telescope[24], and applied the following relation[39]

$$[\mathrm{Fe/H}] = (7.02 \pm 2.10)\Sigma\mathrm{Fe} - 3.97 \pm 2.03 \tag{9}$$

to calibrate it to [Fe/H]. Since the metal-rich and metal-poor populations of Sculptor have been clearly separated on the basis of their metallicity[4], we preferred to work with the iron spectral index rather than with the mean reduced Mg index used in other works[25,10].

To explore further the possibility that our measurement of the anisotropy could be affected by the presence of the different populations in Sculptor, we repeat the procedure outlined above to determine the value of $\hat{\beta}^{MR} = \beta^{MR}(\hat{r}^{MR})$ where again $\hat{r}^{MR} \in [R_{HST}, r_{\rm max}^{MR})$, now using sample that includes only stars with [Fe/H]$\geq -1.4$ dex. To enlarge the statistics, we also include 5 fainter, similarly metal-rich stars. For this sample we find $\hat{\beta}_{\rm MAP}^{MR} = 0.95^{+0.04}_{-0.27}$, a value that is much more tightly constrained that the $\hat{\beta}_{\rm MAP}$ obtained using the best PM sample without a metallicity cut (compare Fig. 4b and 4c in the main body of the paper). The reason for this is not a decrease in the errors (the data satisfy the same quality criteria), nor different numbers of objects, but the heterogeneity present in our original best PM sample. That is, this sample contained stars drawn from the different components in Sculptor with their own, apparently rather different orbital structure. Unfortunately our sample of metal-poor stars with good PM measurements is too small to make a similar analysis and results in an anisotropy that is relatively unconstrained.

**Data Availability Statement.** The data that support the plots within this paper and other findings of this study are available from the corresponding author upon reasonable request.

## REFERENCES


[31] Anderson, J., & Bedin, L. R. An Empirical Pixel-Based Correction for Imperfect CTE. I. HSTs Advanced Camera for Surveys, *Public. Astron. Soc. Pac.* **122**, 1035-1064 (2010).

[32] Ubeda, L., Anderson, J., Study of the evolution of the ACS/WFC charge transfer efficiency, *STScI Inst. Sci. Rep. ACS 2012-03* (2012).

[33] Anderson, J., & King, I., PSFs, Photometry, and Astronomy for the ACS/WFC, *STScI Inst. Sci. Rep. ACS 2006-01* (2006).

[34] Bellini, A., Anderson, J., van der Marel, R. P., et al. Hubble Space Telescope Proper Motion (HSTPROMO) Catalogs of Galactic Globular Clusters. I. Sample Selection, Data Reduction, and NGC 7078 Results, *Astrophys. J.* **797**, (2014).

[35] Anderson, J. Empirical PSFs and Distortion in the WFC Camera, The 2005 HST Calibration Workshop: Hubble After the Transition to Two-Gyro Mode. **11**, (2006).

[36] Arenou, F., Luri, X., Babusiaux, C., et al. Gaia Data Release 1. Catalogue validation, *Astron. Astrophys.* **599**, (2017).

[37] Trippe, S., Davies, R., Eisenhauer, F., et al. High-precision astrometry with MICADO at the European Extremely Large Telescope, *Mon. Not. R. Astron. Soc.* **402**, 1126-1140 (2010).

[38] Chiaberge, M., Riess, A., Mutchler, M., Sirianni, M., & Mack, J. Mack, J. ACS Charge Transfer Efficiency. Results from Internal and External Tests, The 2005 HST Calibration Workshop: Hubble After the Transition to Two-Gyro Mode. **36**, (2006).

[39] Zinn, R., & West, M. J. The globular cluster system of the galaxy. III - Measurements of radial velocity and metallicity for 60 clusters and a compilation of metallicities for 121 clusters, *Astrophys. J. Suppl.* **55**, 45-66 (1984).

[40] Schönrich, R., Binney, J., & Dehnen, W. Local kinematics and the local standard of rest, *Mon. Not. R. Astron. Soc.* **403**, 1829-1833 (2010).

[41] Binney, J., & Tremaine, S. 2008, Galactic Dynamics: Second Edition, by James Binney and Scott Tremaine. ISBN 978-0-691-13026-2 (HB). Published by Princeton University Press, Princeton, NJ USA (2008).

[42] Tolstoy, E., Irwin, M. J., Helmi, A., et al. Two Distinct Ancient Components in the Sculptor Dwarf Spheroidal Galaxy: First Results from the Dwarf Abundances and Radial Velocities Team, *Astrophys. J. Lett.* **617**, 119-122 (2004).

---

This preprint was prepared with the AAS LaTeX macros v5.2.